Accelerating X-Ray Data Collection Using Pyramid Beam Ray Casting Geometries

Amir Averbuch, Guy Lifschitz, and Yoel Shkolnisky

***Abstract*—Image reconstruction from its projections is a necessity in many applications such as medical (CT), security, inspection, and others. This paper extends the 2-D Fan-beam method in [2] to 3-D. The algorithm, called Pyramid Beam (PB), is based upon the parallel reconstruction algorithm in [1]. It allows fast capturing of the scanned data, and in 3-D, the reconstructions are based upon the discrete X-ray transform [1]. The PB geometries are reordered to fit parallel projection geometry. The underlying idea is to use the algorithm in [1] by porting the proposed PB geometries to fit the algorithm in [1]. The complexity of the algorithm is comparable with the 3-D FFT. The results show excellent reconstruction qualities while being simple for practical use.**

***Index Terms*—Computerized tomography, X-Ray tomography.**

I. Introduction

X-RAY imaging is a critical component in many applications such as medical scans (CT), baggage scanning in airports, material inspection, cars tire inspection, food inspection, biology, electronics, and many more.

In practice, emitters emanating electromagnetic radiation and detectors, which measure the radiation power arrived at them, are used in X-ray tomography. From the power at the detectors, it is possible to reconstruct a 3-D function of the radiance attenuation. The attenuation factor is unique for different materials. Recently, 3-D reconstructions become practical.

In this paper, we present several related methods to accelerate 3-D X-ray data acquisition when only one emitter is used. These methods are based upon the PB geometry. Its performance is compared with the parallel beam geometry. The original (source) image is reconstructed by the application of the inverse X-ray algorithm [1].

All the proposed methods in the paper are based upon careful positioning of multiple detectors to enable simultaneous collection of many rays that are emitted in all directions by one emitter. The acquisition geometries described in this paper are: 1) *Boundary Aligned emitter Pyramid Beam (BAPB)*. 2) *Sliding Boundary Aligned emitter Pyramid Beam (SBAPB)*, which is a variant of the BAPB method in which the detectors are utilized more efficiently. This method reduces the number of detectors. 3) *Mirrored Pyramid Beam (MPB)*, which collects only a portion of the data required for the reconstruction. The rest of the data is collected by mirroring the rays.

The MPB method requires that the emitter is located on planes inside the bounding volume of the object. Therefore, it is applicable for scanning simultaneously several separated objects in different X-ray chambers. The BAPB method has no such restrictions. In Section V-A, we show how to reduce the number of detectors to the minimum dictated by [1], by positioning them on moving boards. This idea is applicable to all the previously mentioned methods. In our implementation, the geometry in each axis is the same, but nevertheless, each axis can have its own geometry.

The proposed PB ray casting topology speeds the 3-D X-ray data acquisition by a factor of $O(n^2)$ in comparison to the parallel beam topology.

The structure of the paper is as follows. Section II reviews related works on fast inversion algorithms of the X-ray transform and fast data acquisition using pyramid beams or cone beams. In Section III, the X-ray transform and its discrete version, which appeared in [1], are described. Section IV describes the parallel beam data acquisition and reconstruction from X-ray data. The pyramid beam projections are defined in Section V, which contains a description of several acquisition methods and how to convert from pyramid beam projection data into parallel projection data.

II. Related Works

Two main approaches are used to reconstruct 3-D volumes from X-ray projections. The first reconstructs separately 2-D slices of the image and then concatenates the slices to form a 3-D image. This requires the image to be static to prevent registration problems. It also may generate discontinuities in the reconstructed 3-D image. The second generalizes the 2-D reconstruction algorithms to 3-D.

One approach for 3-D object segmentation and reconstruction is used in [8], [9]. [10] registers the 2-D slices and then reconstructs the 3-D object. A technique, which improves the quality of 2-D slices and then uses the improved slices to construct the 3-D image via image processing methods, is described in [11], [12].

In this paper, we are interested in accelerating the acquisition while using a fast 3-D X-ray reconstruction algorithm in [1]. Usually, fast 3-D X-ray reconstruction algorithms are based upon the Fourier slice theorem. Some of these algorithms interpolate the polar grid into a Cartesian grid. The Fourier transform is sensitive to interpolation and the reconstructed

Manuscript received June 06, 2009; revised February 13, 2010; accepted June 24, 2010. Date of publication August 05, 2010; date of current version January 14, 2011. The associate editor coordinating the review of this manuscript and approving it for publication was Dr. Rick P. Millane.

A. Averbuch is with the School of Computer Science, Tel Aviv University, Tel Aviv 69978, Israel (e-mail: amir@math.tau.ac.il).

G. Lifschitz and Y. Shkolnisky are with the Department of Applied Mathematics, School of Mathematical Sciences, Tel Aviv University, Tel Aviv 69978, Israel (e-mail: prometheus.the.great@gmail.com, yoelsh@post.tau.ac.il).

Color versions of one or more of the figures in this paper are available online at http://ieeexplore.ieee.org.

Digital Object Identifier 10.1109/TIP.2010.2064328

image suffers from distortions. The filtered back-projection based algorithms overcome this problem but their complexity is $O(n^4 \log n)$ where n is the image resolution in each axis. Accurate reconstruction that does not necessitate interpolation is described in [1] and it is based upon the constructions in [3], [4].

Bresler *et al.* [18] propose an hierarchical algorithm for applying the back-projection of the 3-D Radon transform. Their algorithm is a "native" 3-D algorithm and does not rely on factorization of the 3-D Radon transform into pairs of 2-D Radon transforms, which makes the algorithm independent of the sampling geometry. The algorithm in [18] decomposes each projection into a sum of eight back-projections, each having n^2 plane-integrals projections onto $n^3/8$ volumes. Each volume is one octant of the reconstruction. The algorithms are applied recursively until each octant's size is one voxel. The complexity of the algorithm is $O(n^3 \log n)$.

Another family of reconstruction algorithms is the multilevel inversion algorithms. Those divide the input sinogram to a number of subsinograms that use either exact or approximate decomposition algorithms. The sinograms are repeatedly subdivided until they are represented by one voxel. Then, the inverse transformation is applied to reconstruct the subvolumes. The subvolumes are aggregated to form the final volume. An exact method to decompose the sinograms is described in [13], which also presents a fast algorithm for approximate reconstruction, and a method that combines both.

Maximum likelihood expectation maximization ([14]) is an iterative reconstruction method, in which an initial reconstruction is guessed, and then updated in order to minimize the difference between the projections of the reconstructed image and the measured projections. It describes a cone beam data acquisition method.

An algorithm that decomposes the image's frequency domain into subbands and reconstructs the subbands on a down-sampled grid is given in [17].

Cone beam projection methods, which are based upon accelerating data acquisition by measuring multiple rays emitted simultaneously from a single source, are given in [14]–[16].

This paper proposes a fast acquisition algorithm which is a variation of the cone beam method. The projection is assumed to be a collection of rays that form a pyramid. These rays are sampled simultaneously. The reconstruction algorithm, which is described in [1], is algebraically accurate, preserves the geometric properties of the continuous transforms, and is rapidly invertible.

III. X-Ray Transform

The proposed fast data acquisition methods in this paper are based upon the 3-D X-ray transform geometry, described in [1]. This 3-D transform is outlined here.

The X-ray transform of a 3-D function $f = f(x,y,z)$ is a collection of all line integrals of f over all lines in 3-D space. A line $l = p + t \cdot \vec{\mathbf{d}}$, $t \in \mathbb{R}$, in 3-D space is defined by its direction unit vector $\vec{\mathbf{d}} \in \mathbb{R}^3$ and a point $p \in \mathbb{R}^3$ that the line passes through.

Definition III-1. Direction by Angles: Two angles $\theta, \phi \in \mathbb{R}$ define a unit direction vector $\vec{\mathbf{d}}_{\theta,\phi} \in \mathbb{R}^3$ by rotating the unit vector $\vec{\mathbf{u}}_x = (1,0,0)$ by $-\phi$ around the Y axis, and then rotating the resulting vector by θ around the Z axis. θ is also known as the vector heading and ϕ as the vector elevation. A line in $\mathbb{R}^3$ with direction $\vec{\mathbf{d}}_{\theta,\phi}$ is denoted by $l^p_{\theta,\phi}$.

Definition III-2. Direction by a Point: A point $p_{dir} \in \mathbb{R}^3$ defines a line direction by a unit vector, denoted by $\vec{\mathbf{d}}_{p_{dir}}$, as the vector from that point to the origin (0,0,0). That is, $\vec{\mathbf{d}} = \vec{p}_{dir}/\|\vec{p}_{dir}\|$. A line in $\mathbb{R}^3$ with $\vec{\mathbf{d}}_{p_{dir}}$ is denoted by $l^p_{p_{dir}}$.

Directions by angles and direction by a point are equivalent.

Definition III-3. Line Integral: The line integral of $f(x,y,z)$ over the line $l^p_{\theta,\phi}$, denoted by $\mathsf{LI}^p_{\theta,\phi}$, is $\mathsf{LI}^p_{\theta,\phi} f = \int_{-\infty}^{\infty} f\left(p + t \cdot \vec{\mathbf{d}}_{\theta,\phi}\right) dt$, $\theta, \phi, t \in \mathbb{R}$, $p \in \mathbb{R}^3$.

From these definitions, the X-ray transform of $f(x,y,z)$, denoted by $\mathsf{XR}f$, is the set $\mathsf{XR}f = \left\{ \mathsf{LI}^p_{\theta,\phi} f \mid \theta,\ \phi \in \mathbb{R},\ p \in \mathbb{R}^3 \right\}$.

In a similar way, the line integral of $f(x,y,z)$ over the line $l^p_{p_{dir}}$, denoted by $\mathsf{LI}^p_{p_{dir}}$, is $\mathsf{LI}^p_{p_{dir}} f = \int_{-\infty}^{\infty} f\left(p + t \cdot \vec{\mathbf{d}}_{p_{dir}}\right) dt$, $t \in \mathbb{R}$, $p, p_{dir} \in \mathbb{R}^3$.

By using these definitions, we get that the X-ray transform of $f(x,y,z)$, is equivalently given by $\mathsf{XR}f = \left\{ \mathsf{LI}^p_{p_{dir}} f \mid p_{dir}, p \in \mathbb{R}^3 \right\}$.

Definition III-4. Parallel Projection: A parallel projection of the X-ray transform is a collection of all the computed line integrals that have the same direction. These lines are defined by a specific direction $\vec{\mathbf{d}}_{\theta,\phi}$ or $\vec{\mathbf{d}}_{p_{dir}}$ where $\theta, \phi \in \mathbb{R}$, $p_{dir} \in \mathbb{R}^3$ and an arbitrary $p \in \mathbb{R}^3$. The projection is denoted by $\mathsf{XR}^p_{\theta,\phi} f$ or $\mathsf{XR}^p_{p_{dir}} f$, respectively.

The Fourier slice theorem links between the parallel projections $\mathsf{XR}^p_{\theta,\phi} f, \theta, \phi \in \mathbb{R}, p \in \mathbb{R}^3$, and the Fourier transform. It establishes that the Fourier transform of a parallel projection in the direction $\vec{\mathbf{d}}_{\theta,\phi}$ of a 3-D function $f(x,y,z)$ is the Fourier transform of $f(x,y,z)$ sampled on a hyper-space perpendicular to $\vec{\mathbf{d}}_{\theta,\phi}$ that passes through the origin. Formally, $\widehat{\mathsf{XR}^p_{\theta,\phi} f} = \hat{f}(\xi)$ where $\xi \in \left(\vec{\mathbf{d}}_{\theta,\phi}\right)^{\perp}$ is the hyper-space perpendicular to the vector $\vec{\mathbf{d}}_{\theta,\phi}$, that passes through the origin. In other words, the 2-D Fourier transform of the parallel projection $\widehat{\mathsf{XR}^p_{\theta,\phi} f}$ equals to the 3-D Fourier transform of $f(x,y,z)$ sampled on ξ.

The Fourier slice theorem shows that in order to reconstruct an image from parallel projections, we need to apply the 2-D Fourier transform to the projections, reorganize them in 3-D space to get the Fourier transform of the original image, and then to apply the 3-D inverse Fourier transform to recover the original image. The discrete X-ray transform in [1] provides an $O(n^3 \log n)$ algorithm for accurately reconstructing the 3-D image. It is based upon the reorganization of the Fourier transforms of the projections in the pseudo-polar grid as was explained in [3], [4].

The invertibility of the algorithm [1] and its validity in representing discrete volumes are proven there in details. Here is a description of how to discretize the image and the underlying pseudo-polar grid (see [3], [4]).

Following are the definitions that describe a discrete image and the sets of points defining the lines directions and their translations. We assume that the image is a discrete 3-D function

$f(x,y,z)$ that is defined as $f=\{f(x,y,z)|-n/2\le x,y,z\le n/2\}$.

According to [1], the projections are separated into three groups. For that, we define,

Definition III-5: ***Main axis,*** denoted A_i, is $X,\ Y,\ Z$ if $i=1,2,3$, respectively, where ***Secondary axes,*** denoted by S_i^1 and S_i^2, are

$$S_i^1\equiv\begin{cases}Y, & i=1\\ X, & \text{otherwise}\end{cases}\qquad S_i^2\equiv\begin{cases}Y, & i=3\\ Z, & \text{otherwise.}\end{cases}$$

The lines in $\mathbb{R}^3$ are also partitioned into three subsets. Each subset is associated with a main axis X,Y or Z. At each subset of lines, the absolute value of the angles between the projections of the lines on the planes XY, XZ and YZ and the main axis A_i are smaller than 45°.

Definition III-6. (Lines Division I): The three subsets of the lines in $\mathbb{R}^3$ are

$$\begin{aligned}L_x=\{&l^p_{\theta,\phi}|-45^\circ\le\theta<45^\circ\text{or}135^\circ\le\theta<225^\circ\\&-45^\circ\le\phi<45^\circ\text{or}135^\circ\le\phi<225^\circ,p\in\mathbb{R}^3\}\\L_y=\{&l^p_{\theta,\phi}|45^\circ\le\theta<135^\circ\text{or}225^\circ\le\theta<315^\circ\\&-45^\circ\le\phi<45^\circ\text{or}135^\circ\le\phi<225^\circ,p\in\mathbb{R}^3\}\\L_z=\{&l^p_{\theta,\phi}|\quad 0^\circ\le\theta<360^\circ,45^\circ\le\phi<135^\circ\text{or}\\&225^\circ\le\phi<315^\circ,p\in\mathbb{R}^3\}.\end{aligned}$$

Loosely speaking, lines that belong to L_i are "closer" to the main axis A_i than to any other axis. This division covers all the lines in $\mathbb{R}^3$—see proof in [1].

Lemma III-7: $l^p_{\theta,\phi}\equiv l^p_{\theta,\phi+180^\circ}\equiv l^p_{\theta+180^\circ,-\phi}$.

From Lemma III-7, Definition III-6 becomes:

Definition III-8. (Lines Division II): The three subsets of the lines in $\mathbb{R}^3$ are

$$\begin{aligned}L_x&=\{l^p_{\theta,\phi}|-45^\circ\le\theta<45^\circ,-45^\circ\le\phi<45^\circ,p\in\mathbb{R}^3\}\\L_y&=\{l^p_{\theta,\phi}|45^\circ\le\theta<135^\circ,-45^\circ\le\phi<45^\circ,p\in\mathbb{R}^3\}\\L_z&=\{l^p_{\theta,\phi}|0^\circ\le\theta<360^\circ,45^\circ\le\phi<135^\circ,p\in\mathbb{R}^3\}.\end{aligned}$$

As explained in Definition III-3, a line integral is defined by a direction and a point the line passes through. The limitations on the directions of the lines that participate in the discrete X-ray transform, are given in Definition III-8. Lemma III-9 determines the minimal set of points required to define lines that produce nontrivial line integrals.

Lemma III-9. ([1]): Assume that each of the coordinates $x,\ y,\ z$ of the function $f(x,y,z)$ are spatially bounded by the interval $[-n/2,n/2]$. In addition, we restrict the directions to the set defined in III.8. Then, the minimal set of points, which is required to define the nontrivial line integrals, includes points with coordinate $A_i=0$ and the coordinates S_i^1 and S_i^2 are bounded by $[-n,n]$. The lines pass through these points as was described in Definition III-3.

Definition III-10: Denote by P^i_{tr} the discrete subset of points of Lemma III-9 that have the coordinates $A_i=0$ and $S_i^1,S_i^2\in\{-n,\dots,n\}$.

Definition III-11: L_i are defined for each A_i by $L_x,\ L_y,\ L_z$ if $i=1,2,3$, respectively.

The collection of nontrivial line integrals over lines from L_i, $i=1,2,3$, is denoted by XR_x XR_y and XR_z, respectively.

For a point $p_{dir}\in\mathbb{R}^3$, Definition III-2 describes how to determine the line direction. In order to discretize the lines sets in Definition III-8, a discrete set of points is defined.

Definition III-12. Discrete Set of Directions: A discrete set of points, denoted by P^i_{dir}, which includes points with the coordinate $A_i=-n/2$ and $S_i^1,S_i^2\in\{-n/2,\dots,n/2\}$, defines a discrete subset of the line set L_i, $i=1,2,3$.

For all the points in P^i_{tr}, the coordinate A_i is equal to 0. Similarly, for all the points in P^i_{dir}, A_i is equal to $-n/2$. Therefore, these points can be defined uniquely by pairs of values from the other two coordinates S_i^1 and S_i^2. This leads to the following definition.

Definition III-13. Simplified Directions and Translations Sets: The points in the sets P^i_{tr} and P^i_{dir} are defined uniquely by the pairs (s,t) and (k,l), respectively, $s,t,k,l\in\mathbb{R}$. k and s represent the coordinate S_i^1 while l or t represent the coordinate S_i^2. These sets of pairs are denoted by $\tilde{P}^i_{tr}$ and $\tilde{P}^i_{dir}$, respectively.

According to [1], the discrete sets P^i_{tr} and P^i_{dir}, $i=1,2,3$, define the set of line integrals required to arrange the data on the pseudo-polar grid. This enables to use the fast and accurate reconstruction method that was described there.

IV. Parallel Projection Geometry

The discrete parallel projections with respect to a main axis A_i are retrieved by restricting the line integrals from Definition III-4 to the set of lines defined by the points in $\tilde{P}^i_{tr}$ and $\tilde{P}^i_{dir}$ (see Definition III-13). For a point $\tilde{p}^i_{dir}\in\tilde{P}^i_{dir}$, the discrete parallel projection $\mathsf{XR}^{\tilde{P}^i_{tr}}_{i,\tilde{p}^i_{dir}}f$, $i=1,2,3$, contains line integrals whose directions are defined by $\tilde{p}^i_{dir}$. For each point $\tilde{p}^i_{tr}\in\tilde{P}^i_{tr}$, there is exactly one line integral in the projection that passes through the point $\tilde{p}^i_{tr}$.

The image is bounded in the interval $[-1,1]$ in each axis. The image resolution at each axis is n. This implies that the set of coordinates $\{-n/2,\dots,n/2\}$ is mapped to $[-1,1]$. The points in the set P^i_{tr}, defined in III.10, have the coordinates $A_i=0$ and $S_i^1,S_i^2\in\{2j/n|j=-n,\dots,n\}$. The points in the set P^i_{dir}, defined in III.12, have the coordinates $A_i=-1$ and $S_i^1,S_i^2\in\{2j/n|j=-n/2,\dots,n/2\}$.

In order to understand where the emitter and detector have to be placed, a specific line is analyzed.

Definition IV-1. Generalized Point Description: $p^i_G(u,v,w)$ is a point where $u,v,w\in\mathbb{R}$ are the coordinates of A_i, S_i^1 and S_i^2, respectively.

Definition IV-2. Generalized Planes: A plane, which is defined by setting the main axis coordinate to a constant value $A_i=c$, $c\in\mathbb{R}$, is denoted by $P_i(c)$.

A line that is defined by the translation point $\tilde{p}^i_{tr}(s,t)$ and by the direction point $\tilde{p}^i_{dir}(k,l)$ passes through the point $p^i_G(0,s,t)$. From Definition III-2, the line direction is $\vec{p}^i_G(-1,k,l)/||\vec{p}^i_G(-1,k,l)||$. Therefore, this line intersects the planes $P_i(1)$ and $P_i(-1)$ at the points $p^i_G(1,s+k,t+l)$ and $p^i_G(-1,s-k,t-l)$, respectively, where $s,t\in\{2j/n|j=-n,\dots,n\}$ and $k,l\in\{2j/n|j=-n/2,\dots,n/2\}$.

The line integrals in the discrete parallel projection are $\mathsf{XR}^{\tilde{P}^i_{tr}}_{i,\tilde{p}^i_{dir}}f$, where $\tilde{p}^i_{dir}$ is a specific point in $\tilde{P}^i_{dir}$ and $\tilde{p}^i_{tr}$ are

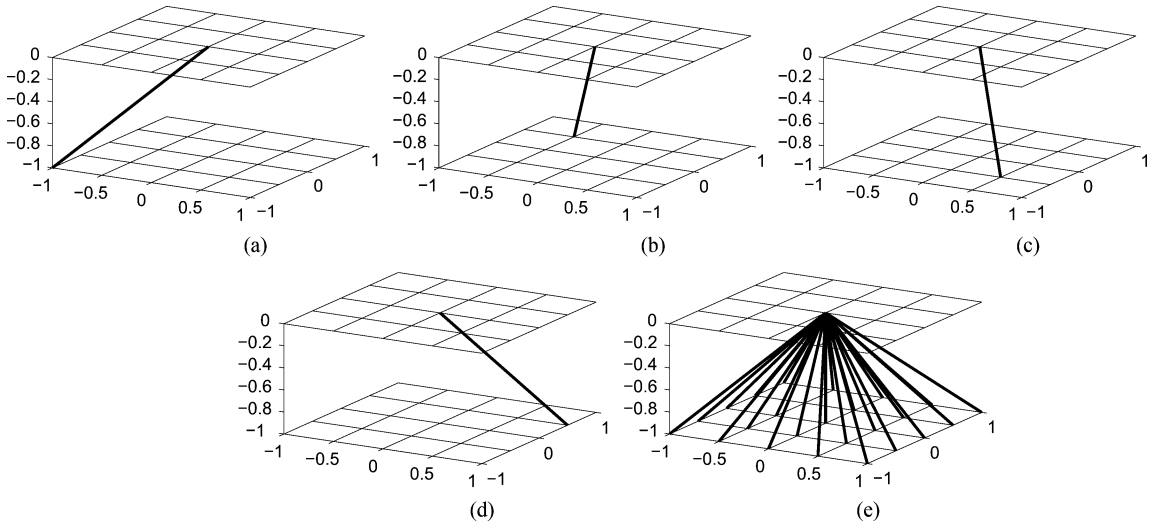

Fig. 1. Lines defined by the point $\tilde{p}^3_{tr}(0,0)$ and by different $\tilde{p}^3_{dir} \in \tilde{P}^3_{dir}$. (a) Line defined by $\tilde{p}^3_{dir}(-1,-1)$. (b) Line defined by $\tilde{p}^3_{dir}(-0.5,0.5)$. (c) Line defined by $\tilde{p}^3_{dir}(0.5,-0.5)$. (d) Line defined by $\tilde{p}^i_{dir}(1,0.5)$. (e) All lines directions defined by the set $\tilde{P}^3_{dir}$.

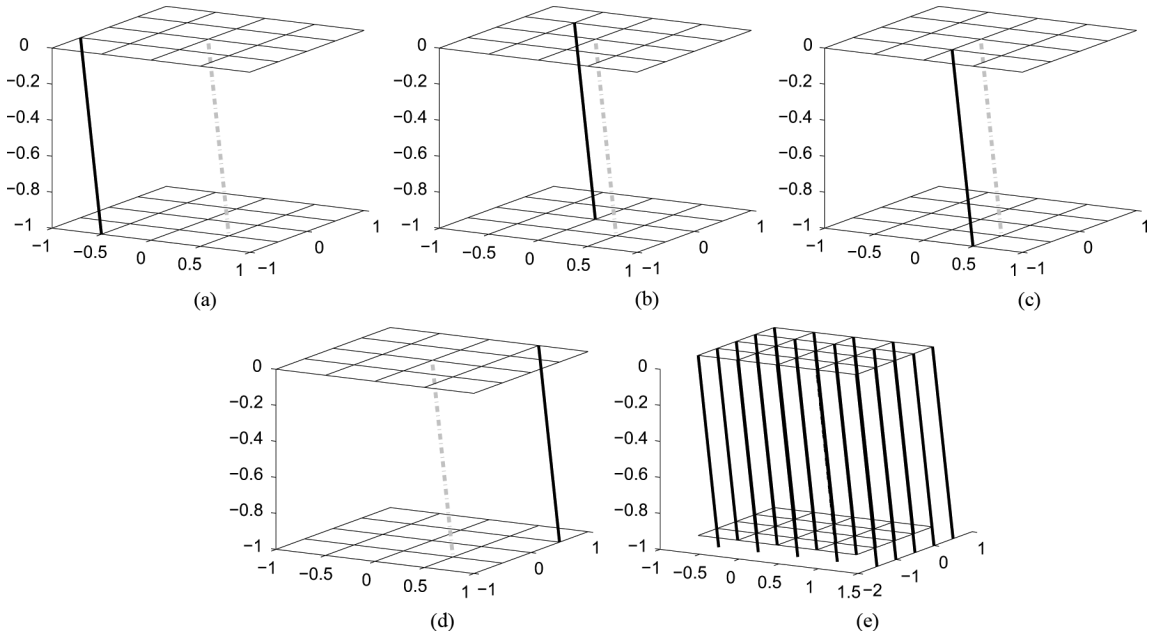

Fig. 2. Lines defined by $\bar{p}^3_{dir}(0.5,-0.5)$ and by different $\bar{p}^3_{tr} \in \bar{P}^3_{tr}$. (a) Line defined by $\bar{p}^3_{tr}(-1.0,-0.5)$. (b) Line defined by $\bar{p}^3_{tr}(-0.5,0.5)$. (c) Line defined by $\bar{p}^3_{tr}(0.0,-0.5)$. (d) Line defined by $\bar{p}^3_{tr}(0.5,1.0)$. (e) Subset of lines from the parallel projection $\mathsf{XR}^{\bar{P}^3_{tr}}_{3,\tilde{p}^3_{dir}(0.5,-0.5)}f$.

all the points in $\tilde{P}^i_{tr}$. Each line passes through a different point on the plane $P_i(0)$. Therefore, the lines are parallel as this method's name suggests.

For a specific direction defined by the point $\tilde{p}^i_{dir}(k,l) \in \tilde{P}^i_{dir}$, the process, which calculates the projection $\mathsf{XR}^{\tilde{P}^i_{tr}}_{i,\tilde{p}^i_{dir}(k,l)}f$ using one emitter, is described in the following. For each point $\tilde{p}^i_{tr}(s,t) \in \tilde{P}^i_{tr}$, the emitter is placed at the point $p^i_G(1,s+k,t+l)$ and the detector is placed at the point $p^i_G(-1,s-k,t-l)$, $k,l \in \{2j/n | j=-n/2,\ldots,n/2\}$ and $s,t \in \{2j/n | j=-n,\ldots,n\}$. The emitter's positions are all in a square where the coordinates $A_i = 1$ and S^1_i, S^2_i are from the interval $[-3.0, 3.0]$. The detectors' positions are the same as the emitter except that $A_i = -1$. This geometry shows that the emitter and the detectors are being located on parallel planes $P_i(1)$ and $P_i(-1)$, respectively.

Fig. 1 shows lines from L_3 (see Definition III-11), which are defined by $\tilde{p}^3_{tr}(0,0)$ and by different points from $\tilde{P}^3_{dir}$. Fig. 2 shows the lines from L_3 which are defined by $\tilde{p}^3_{dir}(0.5,-0.5)$ and by different points from $\tilde{P}^3_{tr}$. In Fig. 2, the gray dashed line denotes the translation $\tilde{p}^3_{tr}(0,0)$. Fig. 3 describes several subsets of lines from parallel projections at different directions.

According to Lemma III-9 and the fact that $f = f(x,y,z)$ is bounded in each direction, it is easy to verify that line integrals over lines with translation greater than 2.0 in one of the dimensions are equal to 0.

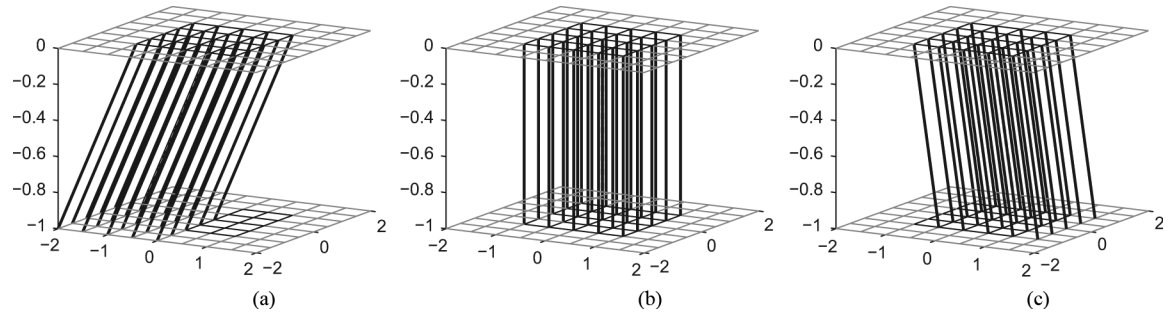

Fig. 3. Parallel projections. A subset of the projection (a) $\mathsf{XR}^{\tilde{P}^3_{tr}}_{3,\tilde{p}^3_{dir}(-1.0,-1.0)}f$, (b) $\mathsf{XR}^{\tilde{P}^3_{tr}}_{3,\tilde{p}^3_{dir}(0.0,0.0)}f$, and (c) $\mathsf{XR}^{\tilde{P}^3_{tr}}_{3,\tilde{p}^3_{dir}(0.5,0.0)}f$.

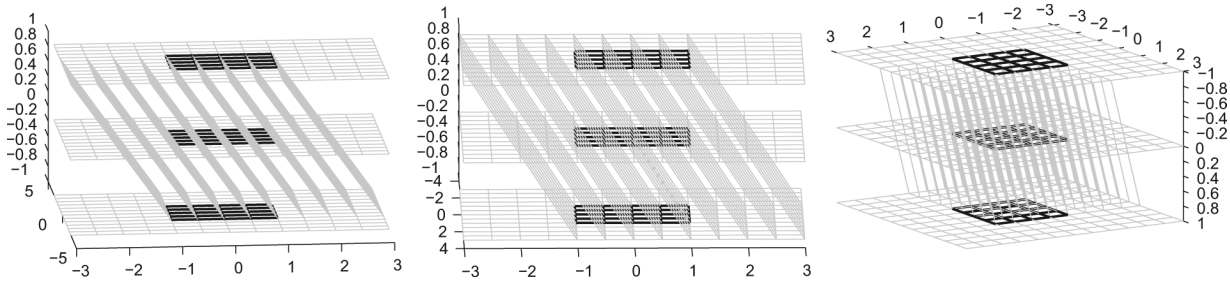

Fig. 4. Different views of lines with the same direction $\bar{p}^3_{dir}(1.0, 1.0)$. The emitter is located on the plane $P_3(1)$ and the detector is located on the plane $P_3(-1)$.

Fig. 4 describes the parallel projection $\mathsf{XR}^{\tilde{P}^3_{tr}}_{3,\tilde{p}^3_{dir}(1.0,1.0)}f$. The bold lines in Fig. 4 represent the bounding volume of $f(x,y,z)$. The gray lines begin in the plane $P_i(1)$ where the emitter is located and end in the plane $P_i(-1)$ where the detector is located. The figure shows that the emitter's and the detector's coordinates S^1_i and S^2_i, respectively, are in the interval $[-3,3]$, as was mentioned earlier.

From Definition III-10, $\tilde{p}^3_{tr} \in \tilde{P}^3_{tr}$ are points on the plane $P_3(0)$. Fig. 4 shows that the coordinates S^1_i and S^2_i of the points on the plane $P_3(0)$ are in the interval $[-2.0,\ 2.0]$. It also shows that lines, which are defined by the points $\tilde{p}^3_{tr}(s,t)$ where s or t equal -2.0 or 2.0, are tangent to the bounding volume. For $|s| > 2$ or $|t| > 2$, the lines do not intersect the bounding volume. These results are also true for projections in directions defined by $\tilde{p}^3_{dir}(k,l)$ where $|k| < 1$ or $|l| < 1$.

The inverse discrete X-ray transform [1] reconstructs the image from a set of parallel projections. The sets P^i_{tr} and P^i_{dir} together define all the line integrals required to reconstruct the image.

Definition IV-3. The Input to the Inverse X-ray Transform: The input to the inverse X-ray transform is all the parallel projections defined by the sets P^i_{tr} and P^i_{dir}. This set, denoted PP, is

$$PP = \left\{ \mathsf{XR}^{p^i_{tr}}_{i,p^i_{dir}} f | p^i_{dir} \in P^i_{dir},\ p^i_{dir} \in P^i_{dir},\ i = 1,2,3 \right\}.$$

The parallel projection $\mathsf{XR}^{\tilde{p}^i_{tr}}_{i,\tilde{p}^i_{dir}} f$ is computed for each direction defined by the point $\tilde{p}^i_{dir} \in \tilde{P}^i_{dir}$. The projection is a 2-D array of size $(2n+1) \times (2n+1)$. The coordinates of each element in the array correspond to a point $\tilde{p}^i_{tr} \in \tilde{P}^i_{tr}$. The value of the array element is $\mathsf{LI}^{\tilde{p}^i_{tr}}_{i,\tilde{p}^i_{dir}} f$.

Definition IV-4. Parallel Projections Data Structure: All the line integrals required to reconstruct the image by the discrete inverse X-ray transform ([1]), are stored in the array PP_{ds}. The first coordinate in the array is i, $i = 1,2,3$, representing the main axis X, Y or Z. The following two coordinates $p,q \in \{1,\ldots,n+1\}$ represent the direction of the line integral $\tilde{p}^i_{dir}(k,l)$ where $k = (p - n/2 - 1) \cdot 2/n$ and $l = (q - n/2 - 1) \cdot 2/n$. The last two coordinates, $u,v \in \{1,\ldots,2n+1\}$, represent the translation of the line integral, $\tilde{p}^i_{tr}(s,t)$ where $s = (u - n - 1) \cdot 2/n$ and $t = (v - n - 1) \cdot 2/n$. Formally

$$PP_{ds}(i,p,q,u,v) = \mathsf{LI}^{\tilde{p}^i_{tr}(s,t)}_{i,\tilde{p}^i_{dir}(k,l)} f. \tag{1}$$

For specific i, p, q and all $u,v \in \{1,\ldots,2n+1\}$, the collection of $PP_{ds}(i,p,q,u,v)$ values is the parallel projections $\mathsf{XR}^{\tilde{P}^i_{tr}}_{i,\tilde{p}^i_{dir}(k,l)} f$ where $k = (p - n/2 - 1) \cdot 2/n$ and $l = (q - n/2 - 1) \cdot 2/n$.

In order to measure a parallel projection in a given direction, the emitter and the detector have to be positioned at $(2n+1)^2$ locations. It means that each parallel projection requires $(2n+1)^2$ operations. For each main axis A_i, $i = 1,2,3$, there are $(n+1)^2$ parallel projections that correspond to different directions. Thus, filling the data structure PP_{ds} requires $3(2n+1)^2(n+1)^2$ operations. Therefore, the total number of operations is $O(n^4)$ where n is the resolution of each dimension.

V. Pyramid-Beam (PB) Reconstruction

The PB data acquisition geometry suggests to use one emitter and add detectors in order to collect simultaneously the line integrals in multiple directions. Line integrals in all directions are measured simultaneously. Therefore, the number of operations required to collect the projection data is divided by $O(n^2)$.

In this section, a family of methods, which are based upon PB geometry, is described. For two constants $c_1, c_2 \in \mathbb{R}, c_1 \neq c_2$, PB projections are computed by locating the emitter on the

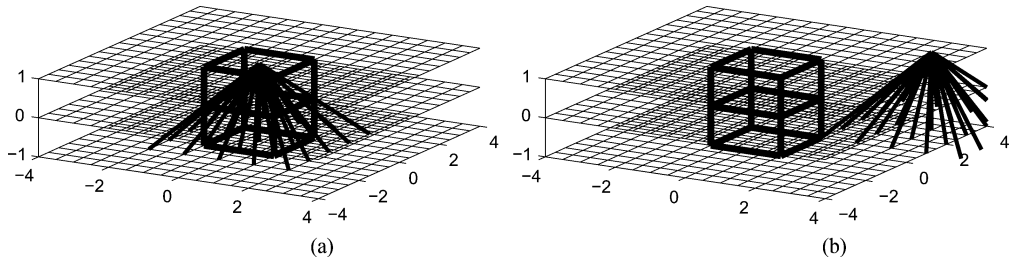

Fig. 5. Different emitter's positions in the $BAPB$ geometry. (a)$BAPB$ projection. (b) Emitter located at $p^3_G(1.0, 3.0, 3.0)$.

plane $P_i(c_1)$ (see Definition IV-2) and the detectors on the plane $P_i(c_2)$. For different PB methods, c_1 and c_2 have different values. This geometry allows a simultaneous acquisition of multiple different line integrals that pass through the same point and have different directions.

The planes $P_i(c_1)$ and $P_i(c_2)$ are parallel. Therefore, the lines participating in each PB projection form a shape of a square pyramid. PB projection is defined in a similar way to Definition III-4.

Definition V-1. PB Projection: A PB projection of the X-ray transform is a collection of all the computed line integrals that pass through a specific point $p \in \mathbb{R}^3$ and have arbitrary directions $\vec{\mathbf{d}}_{\theta,\phi}$ or $\vec{\mathbf{d}}_{p_{dir}}$ where $\theta, \phi \in \mathbb{R}, p_{dir} \in \mathbb{R}^3$. This projection is denoted by $\mathsf{XR}^p_{\theta,\phi} f$ or by $\mathsf{XR}^p_{p_{dir}} f$.

A PB projection $\mathsf{XR}^{\tilde{p}^i_{tr}}_{i,\tilde{P}^i_{dir}} f, i = 1, 2, 3$, is a collection of line integrals defined by a specific point from the set $\tilde{p}^i_{tr}$ and by all the points from the set $\tilde{p}^i_{dir} \in \tilde{P}^i_{dir}$ (see Definition III-13).

The main goal of this paper is to find an efficient method to collect simultaneously multiple line integrals. In order to reconstruct the image by the inverse X-ray transform [1], the PB projections have to be transformed into the PP_{ds} data structure defined by (1). This transformation is called reordering. Each data acquisition method has its own version of reordering algorithm.

The idea is that the algorithm in [1] is efficient and accurate and so each acquisition method with a different PB geometry is transformed into the parallel projection methodology described in Definition III-4.

Several PB methods called $BAPB$, $SBAPB$, and MPB are presented here (see also Section I). For each method, its data acquisition geometry and its reordering algorithm are described, and its complexity is analyzed.

A. Boundary Aligned Pyramid Beam $(BAPB)$ Acquisition Geometry

In BAPB we place the emitter on the planes $P_i(1)$. To measure line integrals with different directions that pass through the same point in the $BAPB$ geometry, the emitter is moved in the plane $P_i(1)$. Multiple detectors are located on an equally spaced grid in a square in the plane $P_i(-1)$. Then, only a subset of the detectors' values, which correspond to line integrals whose slopes are bounded by $[-1, 1]$, are stored in the $BAPB$ data structure (see Definition V-4). Fig. 5 displays the pyramid geometry of BAPB. The tip of the pyramid is on the plane $P_i(1)$.

The two points $\tilde{p}^i_{tr}(s,t) \in \tilde{P}^i_{tr}$ and $\tilde{p}^i_{dir}(k,l) \in \tilde{P}^i_{dir}$ define a line. This line intersects the plane $P_i(1)$ at the point $p^i_G(1, s+k, t+l)$. A second line with a different direction $\tilde{p}^i_{dir}(q,r)$, which passes through the point $p^i_G(1, s+k, t+l)$, intersects the planes $P_i(0)$ and $P_i(-1)$ at the points $p^i_G(0, s+k-q, t+l-r)$ and $p^i_G(-1, s+k-2\cdot q, t+l-2\cdot r)$, respectively. Therefore, the second line is defined by the points $\tilde{p}^i_{tr}(s+k-q, t+l-r)$ and $\tilde{p}^i_{dir}(q,r)$. Since $-1 \le q, r \le 1$, the detectors' secondary coordinates satisfy $s+k-2 \le S^1_i \le s+k+2$ and $t+l-2 \le S^2_i \le t+l+2$, $-2 \le s, t \le 2$ and $-1 \le k, l \le 1$. Therefore, the locations of the detectors that are required to collect the line integrals in the set PP, have the coordinates $A_i = -1$, $-5 \le S^1_i, S^2_i \le 5$. The emitter's positions have the coordinates $A_i = 1$, $-3 \le S^1_i, S^2_i \le 3$.

This geometry requires to position the emitter at $(3n+1)^2$ locations while spreading $(5n+1)^2$ detectors on the plane $P_i(-1)$. From these $(5n+1)^2$ detectors, only $(n+1)^2$ detectors' values represent line integrals from the set PP. How to select these detectors? Two points from the set $\tilde{P}^i_{dir}$ define two different line directions. Two line integrals with different line directions, which pass through the same point, will be detected by different detectors.

In order to collect the line integrals given in PP (see Definition IV-3), the distance between two neighboring locations of the emitter is $2/n$, since for two lines in a parallel projection, which are defined by the points $\tilde{p}^i_{tr}(s,t)$, $\tilde{p}^i_{tr}(s+1/n, t)$ and $\tilde{p}^i_{dir}(k,l)$, the emitter in the $BAPB$ geometry must be located at $p^i_G(1, s+k, t+l)$ and $p^i_G(1, s+k+1/n, t+l)$. This is illustrated in Fig. 6. The emitter is located at two neighboring locations. The distance between the closest detectors, which contain line integrals from PP in the two $BAPB$ pyramid projections, is the same as in the parallel-beam geometry.

By comparing between the $BAPB$ and the parallel projections geometries, we get that the emitter in both methods is located on the planes $P_i(1)$ with S^1_i and S^2_i coordinates satisfying $-3 \le S^1_i, S^2_i \le 3$.

The $BAPB$ geometry leads to poor utilization of the detectors.

Corollary V-2. Inefficient Detectors Utilization: At each location of the emitter, only $(n+1)^2$ of the $(5n+1)^2$ detectors, are line integral values from the set PP. Moreover, there are no two neighboring detectors which contain values from PP. Either odd or even positioned detectors are used for the reconstruction.

Fig. 6 visualizes Corollary V-2. In Fig. 6(a) and (b), the detectors are placed in the even and odd positions, respectively. Fig. 6(c) shows all the detectors that collect line integrals whose slopes are bounded by $[-1, 1]$.

As was mentioned before, the line integral defined by the points $\tilde{p}^i_{tr}(s,t) \in \tilde{P}^i_{tr}$ and $\tilde{p}^i_{dir}(k,l) \in \tilde{P}^i_{dir}$, intersects the plane

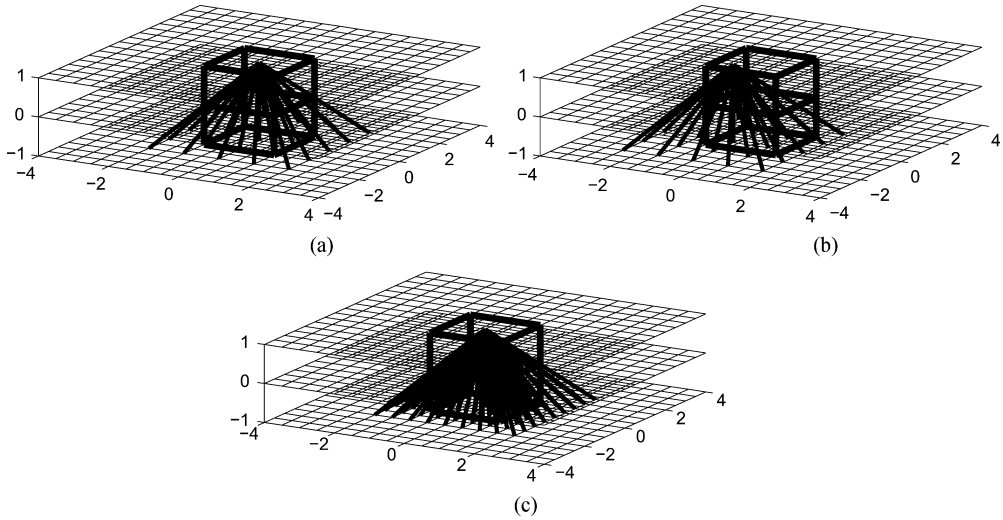

Fig. 6. Detectors' locations for two adjacent emitter's locations in the $BAPB$ geometry. (a) Emitter located at $p_G^3(1.0, 0.0, 0.0)$. (b) Emitter located at $p_G^3(1.0, -0.5, -0.5)$. (c) All line integrals whose slopes are bounded by $[-1, 1]$.

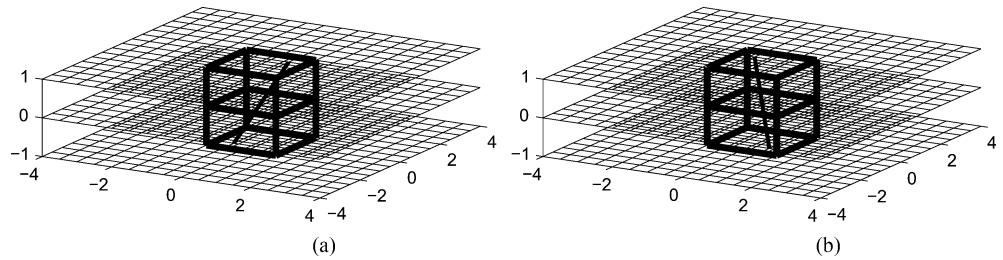

Fig. 7. Translation of the emitter's location in $BAPB$ geometry. (a) Line defined by $\bar{p}_{tr}^3(0.0, 0.0)$ and $\bar{p}_{dir}^3(-0.5, -0.5)$ in the $BAPB$ geometry. (b) Line defined by $\bar{p}_{tr}^3(0.0, 0.0)$ and $\bar{p}_{dir}^3(0.5, -0.5)$ in the $BAPB$ geometry.

$P_i(1)$ at the point $p_G^i(1, s+k, t+l)$. This leads to the following conclusion.

Corollary V-3. Lines From PP, Which Pass Through the Same Point, Appear in Different $BAPB$ Pyramid-Beam Projections: Two line integrals, which are defined by two different directions $\tilde{p}_{dir}^i(k_1, l_1)$ and $\tilde{p}_{dir}^i(k_2, l_2)$ and by one translation $\tilde{p}_{dir}^i(s, t)$, appear in different $BAPB$ projections. These line integrals will appear in the projections where the emitter is located at the points $p_G^i(1, s+k_1, t+l_1)$ and $p_G^i(1, s+k_2, t+l_2)$.

Fig. 7 visualizes Corollary V-3. It shows two lines with a translation that is defined by $\tilde{p}_{tr}^3(0, 0)$. The lines' directions are defined by $\tilde{p}_{dir}^3(-0.5, -0.5)$ and $\tilde{p}_{tr}^3(0.5, -0.5)$. In the $BAPB$ geometry, each line is acquired by a different $BAPB$ pyramid.

The translation of the emitter in the $BAPB$ geometry does not enable to compute the projections in a similar way as was defined in V.1. Instead, the emitter is located in positions where $A_i = 1$, and S_i^1, S_i^2 vary in the interval $[-3, 3]$ with the step $1/n$. For each $S_i^1 = s$ and $S_i^2 = t$, the detectors, whose coordinates are $s - 2 \le S_i^1 \le s + 2$ and $t - 2 \le S_i^2 \le t + 2$, generate the projection.

The projection's result is a 2-D array of size $(2n+1) \times (2n+1)$. The coordinates of each element in the array correspond to a pair (k, l) where $k, l \in \{j/n | j = -n, \ldots, n\}$. This pair represents the direction of the line integral in the same way as the points in the set $\tilde{P}_{dir}^i$. This pair together with the emitter's position $p_G^i(1, s, t)$, $s, t \in \{2j/n | j = -3n/2, \ldots, 3n/2\}$, define the pair $(s - k, t - l)$. The pair $(s - k, t - l)$, represents the emitter's translation point $p_G^i(0, s - k, t - l)$. The points $\tilde{p}_{dir}^i(k, l)$ and $\tilde{p}_{tr}^i(s - k, t - l)$, which are defined by k, l, s and t, can neither be in $\tilde{P}_{dir}^i$ nor in $\tilde{P}_{tr}^i$ (see Definition III-13), respectively. This is due to the fact that half of the detectors' values do not represent line integrals from the set PP (see Definition IV-3). The value of the array element is $\mathsf{LI}_{i,\tilde{p}_{dir}^i(k,l)}^{\tilde{p}_{tr}^i(s-k,t-l)} f$ (see Definition III-3).

Definition V-4. $BAPB$ Data Structure: All the line integrals, computed by the $BAPB$ projections, are stored in $BAPB_{ds}$. Its first coordinate is i, $i = 1, 2, 3$. It represents the main axis X, Y or Z. The following two coordinates, $u, v \in \{1, \ldots, 3n+1\}$ represent the translation of the line integral $\tilde{p}_{tr}^i(s, t)$ where $s = (u - 3n/2 - 1) \cdot 2/n$ and $t = (v - 3n/2 - 1) \cdot 2/n$. The last two coordinates $p, q \in \{1, \ldots, 2n+1\}$ represent the direction of the line integral $\tilde{p}_{dir}^i(k, l)$ where $k = (p - n - 1)/n$ and $l = (q - n - 1)/n$. Formally

$$BAPB_{ds}(i, u, v, p, q) = \mathsf{LI}_{i,\tilde{p}_{dir}^i(k,l)}^{\tilde{p}_{tr}^i(s,t)} f. \tag{2}$$

For specific i, u, v and all $p, q \in \{1, \ldots, 2n+1\}$, the collection of values $BAPB_{ds}(i, u, v, p, q)$ is the $BAPB$ projection $\mathsf{XR}_{i,\tilde{p}_{dir}^i}^{\tilde{p}_{tr}^i(s,t)} f$ where $s = (u - 3n/2 - 1) \cdot 2/n$ and $t = (v - 3n/2 - 1) \cdot 2/n$.

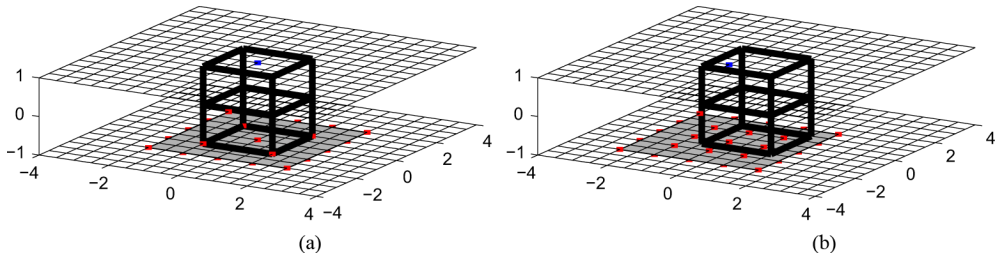

Fig. 8. Sliding detectors positioned on a mobile board that moves together with the emitter. (a) Emitter located at $p^3_G(1.0, 0.0, 0.0)$ in the $SBAPB$ geometry. (b) Emitter located at $p^3_G(1.0, -0.5, -0.5)$ in the $SBAPB$ geometry.

From Corollary V-3 and the $(2n+1)^2$ size of each projction in $BAPB$, we get the reordering algorithm for processing efficiently the $BAPB$ projections.

Lemma V-5. Reordering of the BAPB Dataset: The data in the $BAPB_{ds}$ is reordered to fit the parallel projections geometry by $PP_{ds}(i,p,q,u,v) = BAPB_{ds}(i, u-p+n+1, v-q+n+1, 2\cdot p-1, 2\cdot q-1)$, where $i = 1,2,3, p,q \in \{1,\ldots,n+1\}$ and $u,v \in \{1,\ldots,2n+1\}$. The pair (p,q) represents the parallel projections directions $\tilde{p}^i_{dir}(k,l)$ where $k = (p-n/2-1)\cdot 2/n$ and $l = (q-n/2-1)\cdot 2/n$. The pair (u,v) represents the parallel projections translation $\tilde{p}^i_{tr}(s,t)$, where $s = (u-n-1)\cdot 2/n$ and $t = (v-n-1)\cdot 2/n$.

Proof: A line with the direction $\tilde{p}^i_{dir}(k,l)$, which passes through the point $\tilde{p}^i_{tr}(s,t)$, intersects the plane $P_i(1)$ at the point $p^i_G(1, s-k, t-l)$. Therefore, the coordinates $u,v \in \{1,\ldots,2n+1\}$ are transformed to the coordinates in $BAPB_{ds}$ representing the position $p^i_G(1, s-k, t-l)$. The range of the translation indices in PP_{ds} is $[1, 2n+1]$. The range of the emitter's coordinates S^1_i and S^2_i is $[-2, 2]$. The range of the directions indices in PP_{ds} is $[1, n+1]$. The slopes' ranges are bounded by $[-1, 1]$. A linear mapping of these ranges shows that $s = 2(u-1-n)/n$ and $k = 2(p-1-n/2)/n$. Therefore, $s-k = 2(u-1-n)/n - 2(p-1-n/2)/n = 2/n(u-p-n/2)$. Translation of the range $[-3, 3]$ of the emitter's positions back to the range $[1, 3n+1]$ of the indices, shows that the new index, which represents the coordinate S^1_i of the emitter, is $2/n(u-p-n/2)\cdot n/2 + 3n/2 + 1 = u-p+n+1$. The second coordinate is transformed similarly. The indices, which represent the $BAPB_{ds}$ direction, are doubled and then 1 is subtracted since only the odd indices of the projection belong to the set of line integrals in PP, as was shown in Corollary V-2. ∎

For each main axis A_i there are $(3n+1)^2$ $BAPB$ projections. At each emitter's location, all $(5n+1)^2$ line integrals are measured simultaneously. Only $(n+1)^2$ line integrals from each projection are used. Therefore, computing the data structure $BAPB_{ds}$ requires $3(3n+1)^2$ operations, i.e., $O(n^2)$ operations.

B. Sliding Boundary Aligned Pyramid Beam ($SBAPB$) Acquisition Geometry

In order to overcome the low detectors utilization in the $BAPB$ method, a variation of the method is suggested. This variation uses only $(n+1)^2$ detectors. These detectors are located on a moving board. The distances between the detectors are doubled in order to collect only line integrals from the set PP. In order to collect the correct data when the emitter moves to its next position, the board with the detectors moves together with the emitter. Therefore, the detectors' coordinates S^1_i and S^2_i change at the same amount as the emitter's coordinates S^1_i and S^2_i. This setting reduces the number of required detectors by a factor of 25 and, thus, it provides a full utilization of the detectors.

This setting is called Sliding Boundary Aligned Pyramid Beam ($SBAPB$). Fig. 8 shows detectors (marked in red) which are placed on a moving board (marked as gray rectangle). The detectors' distances are doubled. The right figure shows how the board moves together with the emitter (marked in blue).

When $SBAPB$ is used, the projections become $(n+1)\times(n+1)$ arrays. All the data elements in these arrays contain valuable data. The reordering transform becomes: $PP_{ds}(i,p,q,u,v) = BAPB_{ds}(i, u-p+n+1, v-q+n+1, p, q)$ where i, p, q, u and v are the same as in Lemma V-5.

The time complexity of the $SBAPB$ data acquisition method is the same as the $BAPB$ complexity since there is no difference between these methods except for the number of line integral being calculated simultaneously. The memory complexity is also $O(n^2)$ but it is reduced by a factor of 25.

C. Mirrored Pyramid Beam (MPB) Acquisition Geometry From Multiple Objects

Another set of detectors is placed on the planes $P_i(1)$. This set represents the mirror image of the original set with respect to planes $P_i(0)$. The rays emitted from an emitter at $P_i(0)$ are detected by this new set of detectors, and form a mirror image of the original pyramid [the gray pyramid in Fig. 10(a)]. Due to the symmetry of the original pyramid, each line integral in the original pyramid has its line extension in the mirrored pyramid. The sum of the line integrals is the complete line integral through the scanned object [see Fig. 9(a) and (b)].

Definition V-6. MPB Data Structure: All the line integrals, which are required to reconstruct the image by the discrete inverse X-ray transform [1], are stored in the arrays MPB^-_{ds} and MPB^+_{ds}. The first coordinate in each array, $i = 1,2,3$, represents the main axis X, X or Z. The following two coordinates $u,v \in \{1,\ldots,2n+1\}$ represent the translation of the line integral, $\tilde{p}^i_{tr}(s,t)$ where $s = (u-n-1)\cdot 2/n$ and $t = (v-n-1)\cdot 2/n$. The last two coordinates, $p,q \in \{1,\ldots,n+1\}$

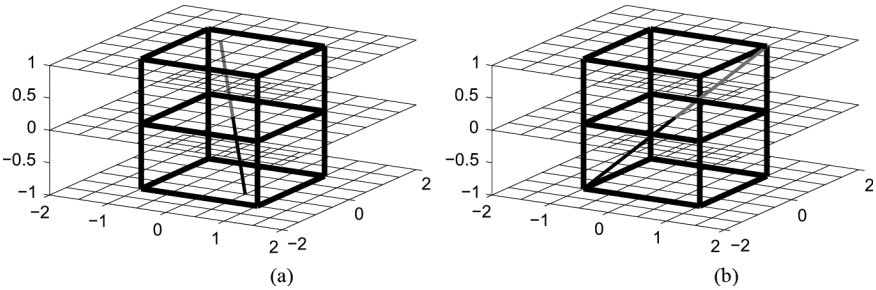

Fig. 9. Line integrals calculated with the MPB geometry. (a) Line integrals defined by $\bar{p}^3_{dir}(-0.5, 0.5)$ and $\bar{p}^3_{tr}(0.0, 0.0)$. (b) Line integrals defined by $\bar{p}^3_{dir}(-1.0, -1.0)$ and $\bar{p}^3_{tr}(0.0, 0.0)$.

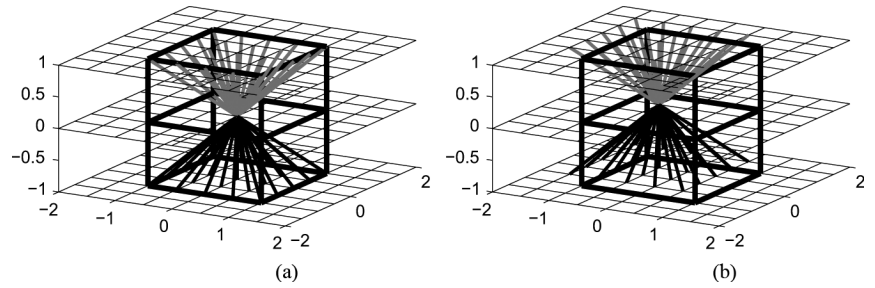

Fig. 10. MPB geometry. (a) Emitter is located at $\widetilde{p}^3_{tr}(0, 0)$. (b) Emitter is located at $\widetilde{p}^3_{tr}(-0.5, 0.5)$.

represent the direction of the line integral $\tilde{p}^i_{dir}(k, l)$ where $k = (p - n/2 - 1) \cdot 2/n$ and $l = (q - n/2 - 1) \cdot 2/n$. Formally

$$MPB^-_{ds}(i, u, v, p, q) = \mathsf{LI}^{\tilde{p}^i_{tr}(s,t)}_{i,\tilde{p}^i_{dir}(k,l)} f^-_i$$
$$MPB^+_{ds}(i, u, v, p, q) = \mathsf{LI}^{\tilde{p}^i_{tr}(s,t)}_{i,\tilde{p}^i_{dir}(k,l)} f^+_i \tag{3}$$

where f^-_i is the portion of the function $f(x, y, z)$ between the planes $P_i(0)$ and $P_i(-1)$, and f^+_i is the portion of the function $f(x, y, z)$ between the planes $P_i(0)$ and $P_i(1)$.

Lemma V-7. Reordering the MPB Data Structure: The data in the MPB^-_{ds} and MPB^+_{ds} data structures is reordered into parallel projections by $PP_{ds}(i, p, q, u, v) = MPB^-_{ds}(i, u, v, p, q) + MPB^+_{ds}(i, u, v, p, q)$ where $i = 1, 2, 3$, $p, q \in \{1, \ldots, n + 1\}$ and $u, v \in \{1, \ldots, 2n + 1\}$. The pair (p, q) represents the parallel projections directions $\tilde{p}^i_{dir}(k, l)$, $k = (p - n/2 - 1) \cdot 2/n$ and $l = (q - n/2 - 1) \cdot 2/n$. The pair (u, v) represents the line integrals translations $\tilde{p}^i_{tr}(s, t)$, $s = (p - n - 1) \cdot 2/n$ and $t = (q - n - 1) \cdot 2/n$.

Collecting the line integrals with the MPB method requires $O(n^2)$ operations. $O(n^2)$ additions are required to compute the full line integrals through f. The memory complexity stays $O(n^2)$ while the number of detectors is doubled.

The MPB geometry is based upon the sets of points $\tilde{P}^i_{tr}$ and $\tilde{P}^i_{dir}$ (see Definition III-13). This method can be used to scan simultaneously eight objects with lower resolutions. Putting an object in one of the eight chambers and doubling the number of detectors placed in each plane, can be a substitute for the $BAPB$ method. When it is known that chambers are kept empty, it is possible to reduce significantly the number of the required detectors. Fig. 11 visualizes the quality of the reconstruction.

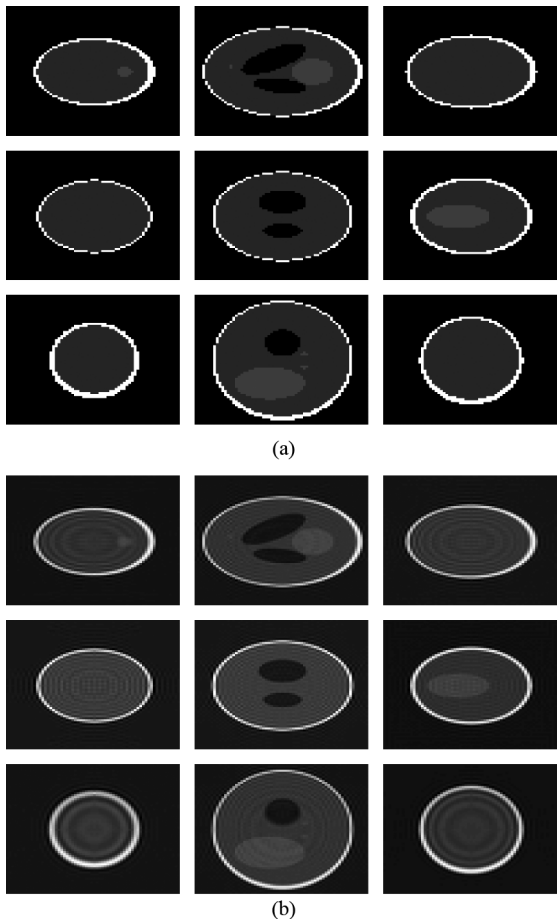

Fig. 11. Reconstructed images (uses analytic projections and inversion from [1]) versus analytic images. $n = 64$. (a) Analytic image with $n = 64$. (b) Reconstructed image with $n = 64$.

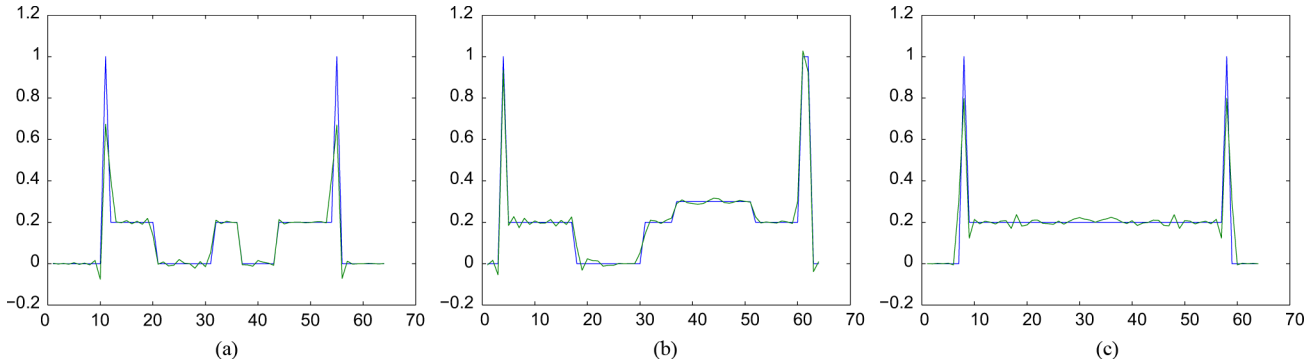

Fig. 12. Comparison between line profiles of the reconstructed image (uses projections that were computed analytically and reconstructed by the application of [1]) and the analytic image. The line profiles in (a), (b), and (c) are $(x, n/2, n/2)$, $(n/2, y, n/2)$, and $(n/2, n/2, x)$, respectively, where $x, y, z = 1, \ldots, n$. The solid lines and the dotted lines represent the line profiles from the analytic image and from the reconstructed image, respectively, for $n = 64$.

TABLE I
$l_{2(diff)}$ IS THE l_2 NORM OF THE DIFFERENCE BETWEEN THE IMAGE THAT WAS RECONSTRUCTED FROM THE ANALYTIC PROJECTIONS USING [1] AND THE ANALYTIC IMAGE. THE PROJECTIONS WERE CALCULATED WITH THE $BAPB$ GEOMETRY

n	$BAPB\ l_{2(diff)}$	$BAPB\ \frac{l_{2(diff)}}{n^3}$
4	0.9	0.014
8	5.182	0.010
16	13.270	0.003
32	36.777	0.001
64	33.372	0.0001
128	68.838	0.00003
256	145.902	0.000009

D. Numerical Results

The performance of the reconstruction algorithm that uses the different acquisitions strategies (described in Sections V-A–V-C) is shown in this section. We sample analytic projections of the 3-D Shepp-Logan phantoms at different resolutions, reconstruct the 3-D object using the 3-D inverse X-ray transform [1], and compare the result to the original Shepp-Logan phantom.

Four different geometries were described in the paper. PP and $BAPB$ are the only ones that have substantially different geometries. The MPB geometry was implemented by computing all the line integrals between the planes $P_i(1)$ and $P_i(-1)$ that pass through the object. The outputs were not separated into two different arrays as was done in the original MPB method.

The numerical outputs from the application of PP and $BAPB$ methods were almost identical. They demonstrate the convergence of the reconstructed image to its analytic image version as the image's resolution increases. The time and memory requirements increase cubically with resolution increase. The algorithms were tested on volumes with resolutions $n = 4,\ 8,\ 16,\ 32,\ 64,\ 128,\ 256$.

Table I shows the decrease of the reconstruction error as the image resolution n in each direction increases. Different acquisition methods generate almost identical results. Therefore, Table I presents only the results from the $BAPB$ method. Fig. 12 shows the profiles of the main axes of the reconstructed image in comparison to the analytic profiles.

E. Conclusion

In Sections V-A–V-C, we described a family of reconstruction algorithms that acquire the scanned data via different PB geometries. These geometries accelerate the data acquisition for X-ray reconstructions that use the method in [1]. All these methods save $O(n^2)$ operations in the data acquisition process by measuring simultaneously line integrals in different directions. All the described geometries are independent of the axes. In our implementation, the geometry in all axes was the same. In other implementations, each axis can have its own geometry. For example, if an object does not intersect the plane where one of the axes is zero, then, we can apply the MPB method only along this axis while applying the $BAPB$ method to the others. Moving boards with detectors can be used in each PB method. This can further reduce the data acquisition costs. Only the PP and $BAPB$ methods where implemented and tested in this paper. Other methods ($SBAPB$ and MPB) will have the same performance and numerical accuracies, since the data are the same and only their ordering is different.

REFERENCES

[1] A. Averbuch and Y. Shkolnisky, "3D discrete X-ray transform," *Appl. Comput. Harmon. Anal.*, vol. 17, pp. 259–276, 2004.
[2] A. Averbuch, I. Sedelnikov, and Y. Shkolnisky, *CT Reconstruction From Parallel and Fan-Beam Projections by 2D Discrete Radon Transform*, submitted for publication.
[3] A. Averbuch, R. Coifman, D. Donoho, and Y. Shkolnisky, "A framework for discrete integral transformations I—The pseudo-polar Fourier transform," *SIAM J. Sci. Comput.*, vol. 30, no. 2, pp. 764–784, 2008.
[4] A. Averbuch, R. Coifman, D. Donoho, Y. Shkolnisky, and I. Sedelnikov, "A framework for discrete integral transformations II—2D discrete Radon transform," *SIAM J. Sci. Comput.*, vol. 30, no. 2, pp. 785–803, 2008.
[5] S. R. Deans, *The Radon Transform and Some of Its Applications*. Hoboken, NJ: Wiley, 1983.
[6] F. Natterer, *The Mathematics of Computerized Tomography*. Hoboken, NJ: Wiley, 1986.
[7] A. Kak and M. Slaney, *Principles of Computerized Tomographic Imaging*. Piscataway, NJ: IEEE Press, 1988.
[8] A. Schenk, G. Prause, and H. O. Peitgen, "Efficient semiautomatic segmentation of 3D objects," *Med. Images*, vol. 1935/2000, pp. 71–131, 2000.
[9] K. S. Shreedhara and S. P. Indira, "Construction of 3-D objects using 2-D cross sectional data and curves," *Adv. Comput. Commun.*, pp. 630–631, 2006.
[10] S. Krinidis, C. Nikou, and I. Pitas, "3D volume reconstruction by serially acquired 2D slices using a distance transform-based global cost function," *Lecture Notes In Computer Science*, vol. 2308, pp. 390–400, 2002.

[11] M. Fano and M. Polák, "The 3D object reconstruction from 2D slices," in *Proc. Central Eur. Sem. Comput. Graph.*, 2000 [Online]. Available: http://www.cg.tuwien.ac.at/hostings/cescg/CESCG-2000/MFano/paper.pdf
[12] G. Lin, U. Adiga, K. Olson, J. F. Guzowski, C. A. Barnes, and B. Roysam, "A hybrid 3D watershed algorithm incorporating gradient cues and object models for automatic segmentation of nuclei in confocal image stacks," in *Cytometry*. Hoboken, NJ: Wiley, 2003, pp. 23–36.
[13] A. Brandt, J. Mann, M. Brodski, and M. Galun, "A fast and accurate multilevel inversion of the radon transform," *SIAM J. Appl. Math.*, vol. 60, no. 2, pp. 437–462, 2000.
[14] K. Mueller, "Fast and accurate three-dimensional reconstruction from cone-beam projection data using algebraic methods," Ph.D. dissertation, Ohio State Univ., Columbus, OH, 1998.
[15] G. Iain, B. Ari, B. Olivier, L. Frank, S. Sebastian, and T. Scott, "Evolution of computer technology for fast cone beam backprojection, computational imaging V," in *Proc. SPIE*, 2007, vol. 6498, p. 64980R.
[16] S. Xiao, Y. Bresler, and D. C. Munson, Jr, "Fast feldkamp algorithm for cone-beam computer tomography," in *Proc. Int. Conf. Image Process.*, 2003, vol. 2, pp. 819–822.
[17] T. Rodet, P. Grangeat, and L. Desbat, "Multichannel algorithm for fast 3D reconstruction," *Phys. Med. Biol.*, vol. 47, no. 15, pp. 2659–2671, 2002.
[18] S. Basu and Y. Bresler, "$O(N^3 \log N)$ backprojection algorithm for the 3-D Radon transform, medical imaging," *IEEE Trans.Med. Imag.*, vol. 21, no. 2, pp. 76–88, Feb. 2002.

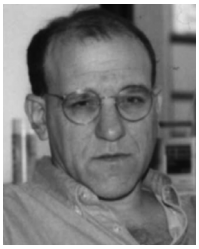

Amir Averbuch received the B.Sc. and M.Sc. degrees in mathematics from the Hebrew University, Jerusalem, Israel, in 1971 and 1975, respectively, and the Ph.D. degree in computer science from Columbia University, New York, in 1983.

In 1987, he joined the School of Computer Science, Tel Aviv University, Tel Aviv, Israel, where he is currently a Professor of computer science. From 1966 to 1970 and 1973 to 1976, he served in the Israeli Defense Forces. From 1976 to 1986, he was a Research Staff Member at IBM T. J. Watson Research Center, Yorktown Heights, New York, Department of Computer Science. His research and development interests include applied harmonic analysis (wavelets, signal/image processing, hyper-spectral processing, high-dimensional processing, and data mining), numerical computation, and scientific computing.

Guy Lifschitz received the M.Sc. degree with honors from the Department of Applied Mathematics, School of Mathematical Sciences, Tel Aviv University, Tel Aviv, Israel, where he is currently pursuing the M.BA. degree.

He is also a project leader in D.V.P. Technologies, Tel Aviv, Israel.

Yoel Shkolnisky received the B.Sc. degree in mathematics and computer science and the M.Sc. and Ph.D. degrees in computer science, all from Tel Aviv University, Tel Aviv, Israel, in 1996, 2001, and 2005, respectively.

From 2005 to 2008, he was a Gibbs Assistant Professor of Applied Mathematics in the Department of Mathematics, Yale University, New Haven, CT. Since 2009, he has been with the Department of Applied Mathematics, Tel Aviv University, Tel Aviv, Israel. His research interests include computational harmonic analysis, scientific computing, and data analysis.